Index Theory-Based Algorithm for the Gradiometer Inverse Problem

Robert C. Anderson and Jonathan W. Fitton

Abstract: We present an Index Theory based gravity gradiometer inverse problem algorithm. This algorithm relates changes in the index value computed on a closed curve containing a line field generated by the positive eigenvector of the gradiometer tensor to the closeness of fit of the proposed inverse solution to the mass and center of mass of the unknown. We then derive a method of determining bounds on the unknownôs center of mass and/or total mass and apply it as a function of gradiometer observables. Both observational errors and the varieties of possible mass distributions generating the gradients are taken into account for the bounds.

Key Words: *Gravity Gradiometer, Inverse Problem, Index Theory*

Mathematics Subject Classification 31A99

R.Anderson J. Fitton

National Geospatial Intelligence Agency, Basic and Applied Research Office, NGA/IB, 3838 Vogel Rd, MS L-64, Arnold, MO, USA 63129

Phone: 314-676-0919

Fax: 314-676-3121

e-mail: Robert.c.anderson@nga.mil

J. Fitton

Phone: 314-676-1208

e-mail: jonathan.w.fitton@nga.mil

Report Documentation Page

Form Approved
OMB No. 0704-0188

1. REPORT DATE	2. REPORT TYPE	3. DATES COVERED
28 MAR 2015	**N/A**	**-**

4. TITLE AND SUBTITLE
Index theory-based algorithm for the gradiometer inverse problem

5a. CONTRACT NUMBER
5b. GRANT NUMBER
5c. PROGRAM ELEMENT NUMBER

6. AUTHOR(S)
Anderson, Robert C., Ph. D. Fitton, Jonathan W., Lt Col

5d. PROJECT NUMBER
5e. TASK NUMBER
5f. WORK UNIT NUMBER

7. PERFORMING ORGANIZATION NAME(S) AND ADDRESS(ES)
National Geospatial-Intelligence Agency, NGA/IB 3838 Vogel Rd, MS L-64, Arnold, MO 63010

8. PERFORMING ORGANIZATION REPORT NUMBER

9. SPONSORING/MONITORING AGENCY NAME(S) AND ADDRESS(ES)

10. SPONSOR/MONITOR'S ACRONYM(S)
11. SPONSOR/MONITOR'S REPORT NUMBER(S)

12. DISTRIBUTION/AVAILABILITY STATEMENT
Approved for public release, distribution unlimited

13. SUPPLEMENTARY NOTES
Published in GEM - International Journal on Geomathematics, 2015, DOI 10.1007/s13137-015-0072-x. Approved for public release, NGA Case # 15-009, The original document contains color images.

14. ABSTRACT
We present an Index Theory based gravity gradiometer inverse problem algorithm. This algorithm relates changes in the index value computed on a closed curve containing a line field generated by the positive eigenvector of the gradiometer tensor to the closeness of fit of the proposed inverse solution to the mass and center of mass of the unknown. We then derive a method of determining bounds on the unknownâs center of mass and/or total mass and apply it as a function of gradiometer observables. Both observational errors and the varieties of possible mass distributions generating the gradients are taken into account for the bounds.

15. SUBJECT TERMS
Gravity gradiometer, inverse problem, index theory

16. SECURITY CLASSIFICATION OF:			17. LIMITATION OF ABSTRACT	18. NUMBER OF PAGES	19a. NAME OF RESPONSIBLE PERSON
a. REPORT	b. ABSTRACT	c. THIS PAGE			
unclassified	**unclassified**	**unclassified**	**UU**	**12**	

Standard Form 298 (Rev. 8-98)
Prescribed by ANSI Std Z39-18

1 Introduction

There has been a surge of interest in application involving gradiometer data recently, particularly gradiometer inverse problems. One main areas of application surrounds gradiometer inverse problems focused on the European Space Agency's geodetic satellite mission, GOCE, and the gravitational gradient observations produced along its orbits. This inverse problem is interested in producing spherical harmonic series representations of the Earth's gravitational potential (Freeden and Nutz 2011; Murböck et al. 2011; Novák and Tenzer 2013). The second main focus area is on geophysical prospecting problems now feasible due to recent improvements in airborne and land gradiometers, such as those available from Lockheed Martin (Difrancesco 2007). Additionally, emerging systems based on atom interferometry show promise at increasing instrument accuracy by an order of magnitude (McGuirk et al. 2002). Also advances in algorithms aimed at modeling the gradients from local terrain and improving the likelihood of solving the local prospecting inverse problem are presented in Jekeli (2012) and Uzun and Jekeli (2015).

The inverse source problem for the gradiometer tensor can be stated generally as follows: given a gradiometer tensor field, extract information about the unknown object from which it was generated. In practice, information about the unknown object is determined by identifying model parameters that generate gradiometer terms at the surveyed locations that are a close fit to the observations. This may be done by some estimation process like least squares or by trying many models (forward modeling) and keeping a ñbest fittingò one. This model is then assumed to have something in common with the unknown object ï location, mass, etc. In Anderson (2011), it was shown that the gradiometer inverse problem reduces to the inverse problem of the potential. Mass distributions of different mass, size, and location can produce very similar external potential fields. Given this nature of the inverse problem, combined with instrument and environmental noise found in practical applications, the inverse solution is often wrong in fundamental ways. That is, the inverse problem in the typical geophysical prospecting setting is usually considered unstable unless certain parameters are highly constrained. In this paper, we present a new theory that specifies when an inverse solution model would have the same center of mass and total mass as the unknown. The total mass estimate includes estimating regions with both negative and positive density contrast. In practical problems, this can help mitigate the pervasive instability problem that can produce false positives/negatives typically caused by not correctly determining the unknown's true center of mass location and total mass. In addition, we derive a bound for the center of mass location and the total mass for strictly positive (or negative) bounded mass anomalies as a function of the supremum norm of the differential curvature.

2 Mathematical Basis

Let $\mu(\mathbf{y})$ be a mass distribution. The **potential function**, U, generated by μ is defined by the Lebesgue integral

$$U(\mathbf{x}) = \int \frac{G d\mu(\mathbf{y})}{|\mathbf{x}-\mathbf{y}|}, \tag{1}$$

where $\boldsymbol{x}$ is a point in space, $\boldsymbol{y}$ is a point in the mass distribution, and G is Newton's gravitational constant.

The Hessian of the potential, $H(U)$, is the tensor field whose components in rectangular coordinates are $U_{ij} = \dfrac{\partial^2 U}{\partial x_i \partial x_j}$. It is often convenient to express H in matrix notation.

$$H = \nabla\nabla^T U = \begin{bmatrix} U_{xx} & U_{xy} & U_{xz} \\ U_{yx} & U_{yy} & U_{yz} \\ U_{zx} & U_{zy} & U_{zz} \end{bmatrix} \tag{2}$$

where $\nabla = \left(\dfrac{\partial}{\partial x}, \dfrac{\partial}{\partial y}, \dfrac{\partial}{\partial z} \right)$ is the gradient operator.

The matrix in Eq. 2 is symmetric and satisfies Laplaceôs equation. Thus, H has only five independent terms and is a symmetric order 2 tensor field outside the support of the mass.

The Partial Tensor gradiometer produces observables comprised of a combination of Hessian terms restricted to the horizontal plane, referred to as the in-line and cross gradients and defined as $P = U_{xx} - U_{yy}$ and $Q = 2U_{xy}$ respectively. There is also a Full Tensor gradiometer that supplies H as the observable, but our work focuses on the Partial Tensor system.

The **Gradiometer Tensor** generated by the mass anomaly μ, denoted GT^{μ}, is the second-order tensor field in the xy-plane defined by

$$GT^{\mu} = P(dx \otimes dx - dy \otimes dy) + Q(dx \otimes dy + dy \otimes dx). \quad 3$$

Note, the gradiometer tensor is a symmetric and trace free (trace = 0) covariant tensor field of order 2 on the xy-plane. Thus, Eq. 3 can be written in matrix notation as

$$GT^{\mu} = \begin{pmatrix} P & Q \\ Q & -P \end{pmatrix} \quad 4$$

From the gradiometer tensor, the **Differential Curvature,** which is the scalar field DC in the plane, is readily calculated as

$$DC = \sqrt{P^2 + Q^2} \quad 5$$

The points where the differential curvature is zero (i.e., $P=Q=0$) are exactly the singularity points of the gradiometer tensor. It was shown in Anderson (2011) that the value of DC does not change with coordinate system rotation or translation, which makes the differential curvature a convenient observable in practical applications.

A simple calculation shows that the eigenvalues of the gradiometer tensor at a given point are $\pm DC$. Since the gradiometer tensor is symmetric at points where it is non-singular, the eigenvectors associated with $+DC$ and ï DC are mutually perpendicular.

Define the **Line Field Λ associated with GT^{μ}** as the line field of GT^{μ} such that $\Lambda(x,y)$ is the eigenspace of GT^{μ} at the non-singular point (x,y) corresponding to the positive eigenvalue $DC(x,y)$. It is convenient to describe the line field by giving the angle $\alpha(x,y)$ that $\Lambda(x,y)$ makes with the x-axis. This angle is called the **azimuthal angle of GT^{μ}** at (x,y). The formula for the azimuthal angle of a gradiometer tensor in terms of its components is the following:

$$\alpha = \begin{cases} 0.5 \tan^{-1} \dfrac{Q}{P} & P \neq 0 \\ \pm \dfrac{\pi}{2} & P = 0 \end{cases} \quad 6$$

The arctangent in Eq. 6 is computed such that the signs of P and Q are accounted for, resulting in an angle that ranges from -´ to +´. Thus, α is on the range of [-´/2, +´/2].

The gradiometer tensor at any point is completely determined by knowing its eigenspace. Thus, by knowing DC and α, we know the tensor itself. The reason for using DC and α is that it allows one to better visualize the gradiometer tensor field.

Now we apply index theory results to the gradiometer tensor line field, and show that the global index value of the line field can provide useful information about the unknown. Background on index theory can be found in section 6.8 in Strogatz (1994) and is summarized below.

If C is a closed curve in the plane which does not pass through any singularities, then the **index of the curve, I_C**, with respect to the field is defined by the line integral

$$I_C = \frac{1}{2\pi} \int_C d\alpha \quad 7$$

Geometrically, the index measures the net rotation of the line field as one goes around the closed curve. The index of an isolated singularity is defined to be the index of any simple closed curve with the usual orientation that surrounds only that singularity. Some properties of the index follow.

1) For any closed curve C, I_C is an integer multiple of 1/2 which is positive if the net rotation is counterclockwise and negative if clockwise.
2) For a simple closed curve, C, with the usual orientation that surrounds only isolated singularities, I_C is the sum of the indices of the singularities.

The line field index is said to be a **global index, I_G,** if the curve C surrounds all of the singularities of the field.

Fig. 1 shows the line field for three point masses at (-2, -1, -2), (0, -2, -2), and (1,1,-2) with masses 0.5, -1.5, and 2 respectively. Areas in which $P<0$ are indicated with a blue 'x' and areas in which $Q<0$ are indicated with a red 'o'. Singularities occur at the intersections of the P=0 and Q=0 contours. Each cycle through ($P>0$, $Q>0$), ($P<0$, $Q>0$), ($P<0$,$Q<0$), ($P>0$,$Q<0$) represents a 180 degree rotation of the line field and an index of 0.5. Progressing through this sequence in the opposite direction indicates a negative singularity with an index of -0.5 Using the perimeter of the plot as the curve C produces two complete cycles and an index of 1, as predicted from Theorem 1 for this unbalanced system. Note that,

if curve *C* were a circle with radius 10 centered at the origin, it would exclude the negative singularity at (0,-15) and indicate an index of 1.5. This result illustrates the importance of ensuring *C* encloses all singularities when determining the global index.

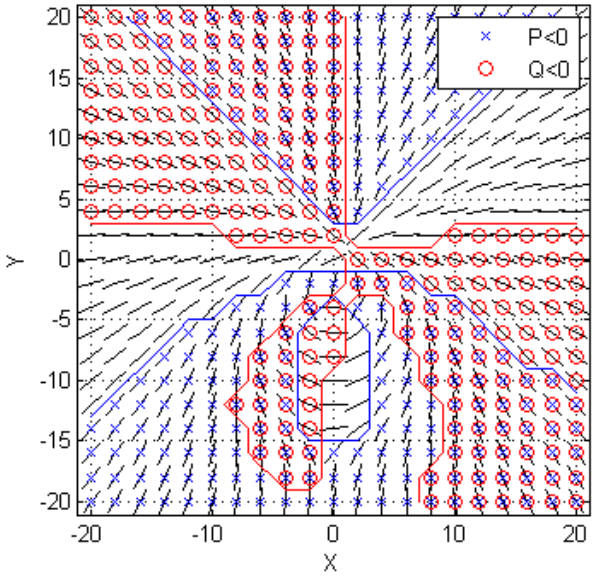

Fig. 1 Example line field for a system of 3 point masses

A **mass anomaly** is the difference between the unknown object and an assumed model (the inverse solution). For a given mass anomaly, the places not modelled correctly can be considered regions of positive or negative mass. Given the mass anomaly, μ, define

$$m^+ = \int d\mu^+, \quad m^- = \int d\mu^-, \tag{8}$$

as the positive and negative parts of the mass anomaly respectively. Define the centers of mass with respect to the *x*-axis for the positive and negative parts of the mass anomaly as

$$\bar{x}^+ = \int \frac{\xi d\mu^+}{m^+}, \quad \bar{x}^- = \int \frac{\xi d\mu^-}{m^-}. \tag{9}$$

The centers of mass with respect to the *y*-axis for the positive and negative parts are similarly defined.

Theorem 1: (1) If $m^+ \neq m^-$ then the global index, $\boldsymbol{I_G}$, equals 1. (2) If $m^+ = m^-$ and $(\bar{x}^+, \bar{y}^+) \neq (\bar{x}^-, \bar{y}^-)$, then $\boldsymbol{I_G}$=3/2.

Corollary 1.1: If $\boldsymbol{I_G}$ is not equal to one, then $m^+ = m^-$; and if $\boldsymbol{I_G}$ is greater than or equal to 2, then $(\bar{x}^+, \bar{y}^+) = (\bar{x}^-, \bar{y}^-)$.

Theorem 1 and its corollary from Anderson (2011) state that if the gradients from the mass anomaly, (i.e., the residual gradients calculated from the difference of the gradients generated by the inverse solution model and the gradients produced by the unknown object) have a global index Ó 2, then the inverse solution has the same total mass and center of mass in *(x,y)* as the unknown. The conditions of Theorem 1 are illustrated in Fig. 2. These plots show the line fields produced by a prism and a cylinder. Formulas used to calculate the gradients from a prism or cylinder can be found in Dransfield (1994) and Romaides et al. (2001) respectively. In Fig. 2a, the cylinder mass is 1.3 times the prism mass and it is offset 3m along the x axis, resulting in an index of 1. In Fig. 2b, the masses are the same, but the cylinder is still offset by 3m, resulting in an index of 1.5. Finally, in Fig. 2c, both the masses and centers of mass of the two objects are the same, resulting in an index of 2. The far left singularity in Fig. 2a has an index of -1/2, while all other singularities have an index of +1/2. This produces an I_G=1 in accordance with Theorem 1.

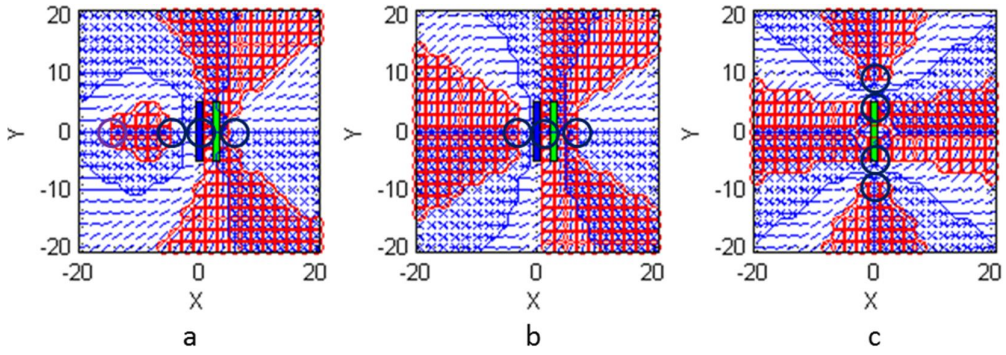

Fig. 2 Line fields for a cylinder and prism with (a) different mass and center of mass, (b) same mass and different center of mass, and (c) same mass and center of mass. The circles represent singularity points where $P=Q=0$.

Theorem 1 and Corollary 1.1 also apply for the vertical planes, P(x,z) and P(y,z). So for certain applications where the anomaly is bounded by areas below both a horizontal and a vertical plane then we get the result for 3D center of mass.

Corollary 1.2: If $\boldsymbol{I_G}$ > 3/2 in any two of the three planes P(x,y), P(x,z), P(y,z) then $(\bar{x}^{+}, \bar{y}^{+}, \bar{z}^{+}) = (\bar{x}^{-}, \bar{y}^{-}, \bar{z}^{-})$, and $m^{+} = m^{-}$.

The following proposition from Anderson (2011) applied with Theorem 1 is used as rationale behind the new algorithm introduced in the next section. For a positive integer N, define the **2N-gon mass anomaly** by placing a mass with sign $(-1)^k$ at the point locations $(\cos(k\pi/N), \sin(k\pi/N), -1)$; ($k$ = 0 é 2N - 1). This anomaly has positive and negative masses that balance and have the same center of mass.

Proposition 1: The global index of the 2N-gon mass anomaly is 1 + N/2.

The line field for a 2N-gon with N=3 is shown in Fig. 3 and has an index of 2.5.

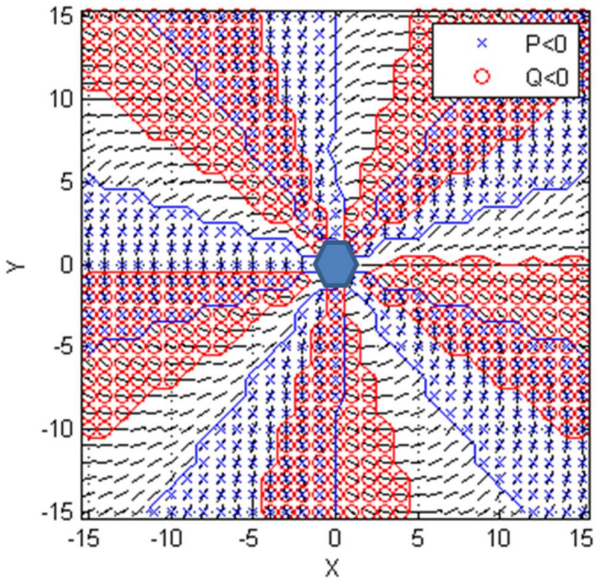

Fig. 3 Line field of a 2N-gon for N=3

3 Results

3.1 Minimum Mass until Bifurcation (MMB) Algorithm

Theorem 1 and its corollaries are extremely sensitive. Very small differences in the mass magnitudes or center of mass locations result in I_G<2. In applied settings, we assume the unknown mass is large

relative to the noise. Additionally, in the applied setting we do not have the luxury of exact observations or surveying great distances from the anomaly to get a global index. However, even in low noise settings, this noise is sufficiently large that we expect a local index of 1.

The pattern produced by the 2N-gon is very unlikely to occur naturally. This makes it useful in conjunction with Theorem 1 for evaluating how accurately a model represents an unknown in terms of its total mass and center of mass. We place a model prism at the hypothesized center of mass of the unknown mass and place a 2N-gon just below the measurement plane and above the center of mass of the model. We then increase the mass on the vertices of the 2N-gon until its distinctive line field pattern emerges at a selected distance from the center of the 2N-gon. We repeat this process while varying the position and dimensions of the model. The model position and dimensions that require the minimum mass on the 2N-gon to produce its distinctive pattern represent the best fit to the unknown. We call this smallest 2N-gon mass required to produce the pattern the **minimum mass until bifurcation** (MMB).

An example result is shown in Fig. 4. The unknown is a rectangular prism 1.25m wide, 1.72m tall, and 15m long with a density of 2300kg/m^3. A model prism of the same length and density is placed at the unknown's center of mass and its width and height are varied in 2cm increments. The resulting surface represents the MMB required on the 2N-gon for each combination of model width and height. As can be seen from the plot, the overall MMB occurs when the model dimensions match those of the unknown. The plot also reveals an arc of local minima. These points represent combinations of width and height which produce models that are similar in total mass.

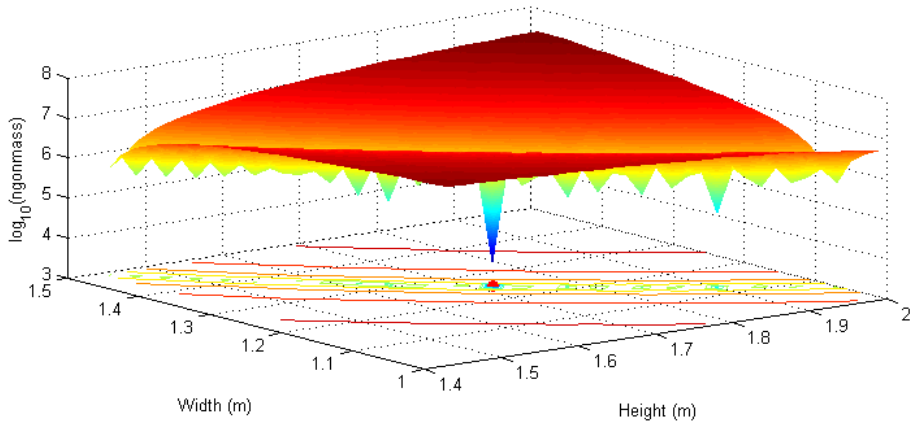

Fig. 4 MMB for a model prism that is a near perfect match in dimensions to the unknown. The large spike occurs at the correct prism dimensions.

If no model perfectly matches the unknown, the MMB may occur anywhere along the arc. For example, if the closest model prism width, length, and height have a 1cm error, result is illustrated in Fig. 5. The largest spike occurs at width 1.32m and height 1.63m.

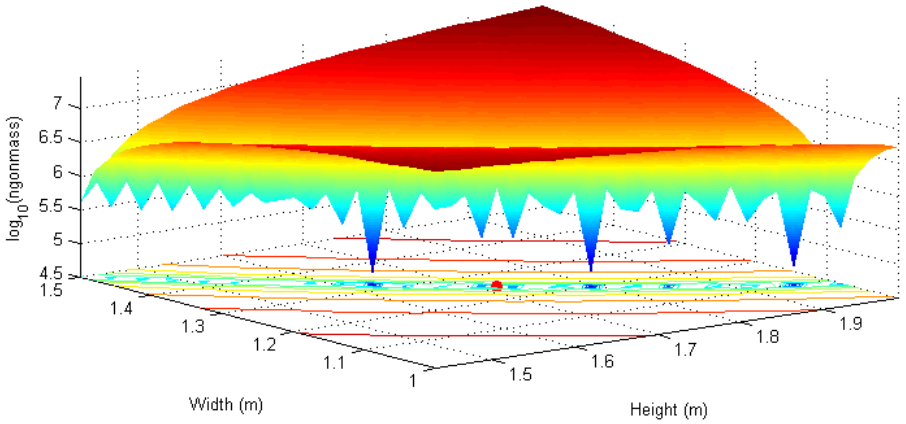

Fig. 5 MMB when no model is a perfect fit. The red dot represents the correct prism dimensions.

The MMB approach can produce inverse solutions very different than those based on an inverse model solution found by minimizing the difference between model generated gradients and the

observed or measured gradients. To demonstrate this, in the next example, the model with the combination of mass and location that minimizes σ_{DC}, the standard deviation of the difference between the *DC* from the point mass model and the observed *DC* of the unknown prism, is compared to MMB point mass solution to the same unknown. This example illustrates the false positive issue often caused when the model has very different shape characteristics than the unknown. In this case the model set can be considered from a family of homogenous balls (point masses), while the unknown is a prism.

In the following figures, we compare inverse solutions for the unknown prism with a point mass and compare the results of the MMB algorithm and the best fit approach computed over increasing distances in the plane above the prism center. We place the point mass at one possible location for the prism center of mass and compute σ_{DC}, the standard deviation of the difference between the *DC* from the point mass model and the observed *DC* of the unknown prism. We then place a 2N-gon above the point mass and determine the MMB. This process is repeated for all combinations of mass and position and identify the combinations that minimize either σ_{DC} or MMB. For both approaches, we evaluate the result over a series of concentric squares to examine how distance from the prism affects the results. If the two methods were equivalent, they would produce the same result. Both methods accurately determine the horizontal center of mass of the prism, but produce different results for its mass and depth. For a 1.0x20x1.5m prism at a depth of 12m with density 2300kg/m^3, Fig. 6 shows σ_{DC} as a function of the point mass/prism mass ratio and the horizontal range from the prism center of mass to the edge of the square area over which σ_{DC} is computed. The minimum σ_{DC} at each range occurs at the largest mass ratio tested. Thus, the inverse solution that most closely fits the observed data yields an incorrect mass of the unknown at all depths tested.

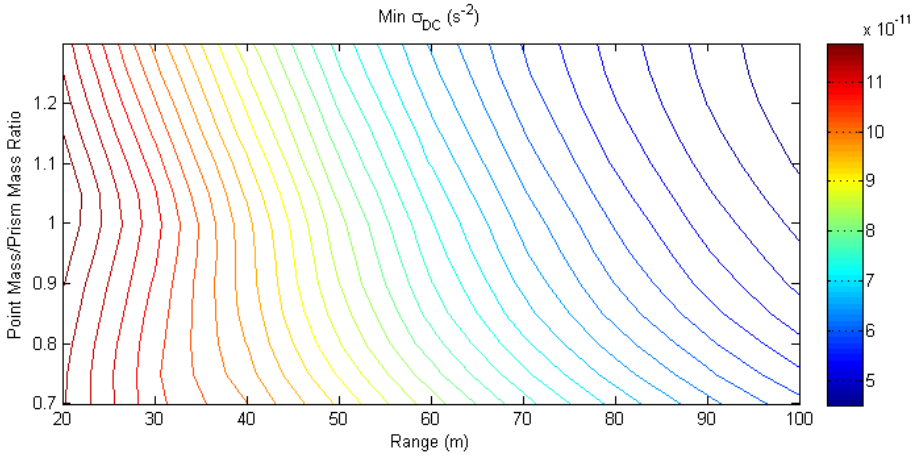

Fig. 6 Best fitting solution using minimum σ_{DC}. The minimum σ_{DC} at each range is at the maximum mass ratio tested and decreases as range increases.

Fig. 7 shows the equivalent result when using the MMB approach. As the range increases, the point mass that minimizes the MMB and the depth error remains consistent.

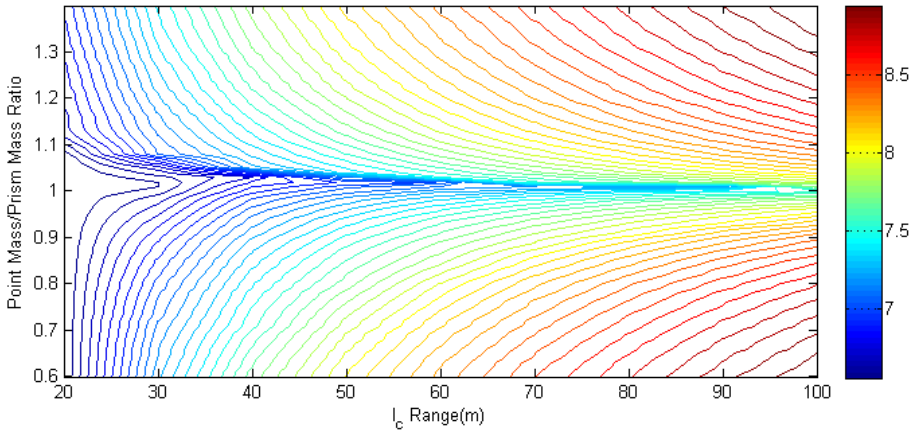

Fig. 7 MMB as a function of range and mass ratio. MMB at each range occurs when model mass equals prism mass

Using this approach of evaluating the MMB computed along a series of increasingly larger concentric squares, it is possible to determine if the model mass is too large or too small. Based on these

observations, we conclude that there is greater confidence in an MMB solution that is stable over increasingly larger ranges.

The magnitude of the MMB can provide some insight into how well the model fits the unknown. In Fig. 8, we replace the point mass used to generate Fig. 7 with a cylinder, which is a much closer fit to the prism. The cylinder's length and density is set to be the same as the prism and its radius is varied. Note that the MMB is lower at the correct ratio with the cylinder than it was for the point mass.

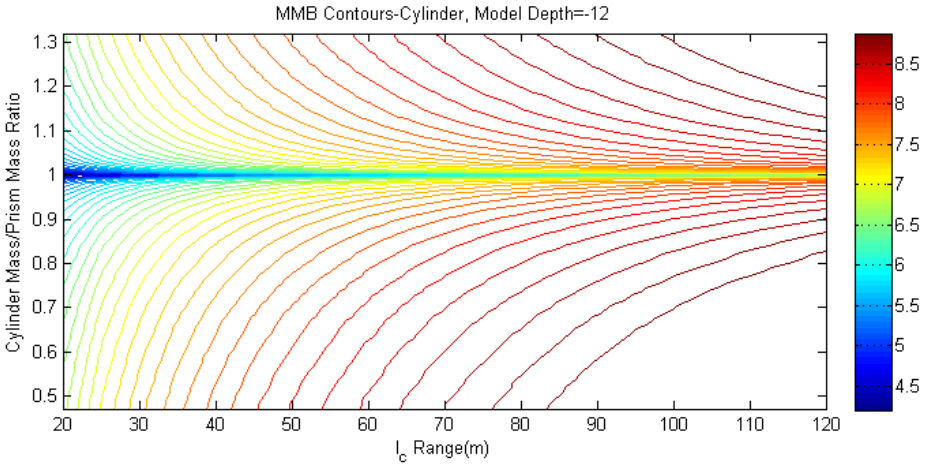

Fig. 8 MMB as a function of range and mass ratio for a cylinder modelling a prism

In a theoretical environment with perfect observations, the MMB solution allows us to find the correct mass and horizontal center of mass of the unknown. However, for practical problems it is very difficult to separate mass and depth. Also, as was illustrated in Fig. 5, multiple inverse solutions of the same mass can be viable candidates for the best fit.

3.2 Mass and Depth Bounds from DC Values

In this section, we derive some fairly sharp bounds on total mass and the center of mass location (depth) of a strictly positive (or negative) unknown mass that are a function of the greatest magnitude of the observed *DC* values (its supremum norm). Our approach takes into account gradient measurement error and mass modeling errors, assuming the unknown is contained within a bounding ball and is strictly positive or negative. If the unknown's location cannot be bounded, then neither the center of mass nor the total mass can be bounded.

Set a unit point mass at depth, *D*, on the z-axis below the (*x, y*) computational plane. Then, symbolically,

$$DC^2 = (U_{xx} - U_{yy})^2 + (2U_{xy})^2 = \frac{9(x^2+y^2)^2}{(x^2+y^2+D^2)^5}. \qquad 10$$

Now, find the maximum *DC* value in the (x, y) plane. Since the *DC* surface plot is rotationally symmetric, we can further simplify Eq. 10 by setting y=0. Then, using methods of Calculus, we take the derivative with respect to *x*, set the result equal to zero, and solve for the roots.

$$\frac{\partial DC_{y=0}}{\partial x} = \frac{3x(-3x^2+2D^2)}{(x^2+D^2)^{\frac{7}{2}}} = 0. \qquad 11$$

The roots of Eq. 11 are $x = \pm D\sqrt{2/3}$. Applying these roots to Eq. 10 with y=0 and inserting the gravitational constant, *G*, and mass, *m*, we get a relationship between the supremum norm for *DC* and the point massôs depth, *D*, and the mass, *m*,

$$\|DC\|_{\sup} = \sup\sqrt{(U_{xx} - U_{yy})^2 + (2U_{xy})^2} = \frac{18\sqrt{3}Gm}{25\sqrt{5}D^3}. \qquad 12$$

As an example of how this equation would be applied, consider the prism used for Fig. 7. The $\|DC\|_{sup}$ for this object is $1.012\text{x}10^{-9}\text{s}^{-2}$ and its mass is $6.9\text{x}10^{4}$kg. Using these values in Eq. 12 and solving for depth produces a result of 13.28m, a 10.6% error for an object quite different from a point mass.

For a quick and simple estimate of the effect of observational error on mass and depth error, we take the derivative of Eq. 12 with respect to mass and depth:

$$d\|DC\|_{\sup} = \frac{18\sqrt{3}G}{25\sqrt{5}D^3}\,dm = -\frac{54\sqrt{3}Gm}{25\sqrt{5}D^4}\,dD. \qquad 13$$

To demonstrate, assume the observational error for *DC* for the preceding example is $\pm 5\text{x}10^{-10}\text{s}^{-2}$. Using the mass of $6.9\text{x}10^{4}$kg and the computed depth of 13.28m, solving Eq. 13 for *dm* and *dD* indicates the mass may vary by $\pm 3.14\text{x}10^{4}$kg and the depth may vary by ±2.02m.

Claim 1. For any mass distribution generating an admissible potential in the (*x, y*) plane, *p*, outside ball, *B*; its $||DC||_{\sup}$ is bounded below by $||DC||_{\sup}$ generated of a uniform ring of unit mass in the equatorial plane of *B* parallel to *p* and bounded above by the $||DC||_{\sup}$ of two point masses, each with mass ½ located at opposite ends of the diameter of *B* (oriented between 0 and 12 degrees off the *z*-axis as *D* increases from 1 to infinity), $||DC||_{\sup,\text{ring}} \le ||DC||_{\sup} \le ||DC||_{\sup,2\text{ pts}}$.

Fig. 9 illustrates the results described in Claim 1. As defined in Green (1952), an admissible potential is generated by a mass distribution within a unit ball where all the mass is contained in the ball, the total mass is 1, and the center of mass is at the center of the ball. We solve Eq. 12 for *D* and compute the depth error for various mass distributions using their calculated *DC*. The horizontal and vertical prisms used for this plot had a 0.04m^2 square cross section and a length that placed their corners on the surface of the ball. The errors converge toward 0 as depth increases and the mass distribution more resembles a point mass from the plane.

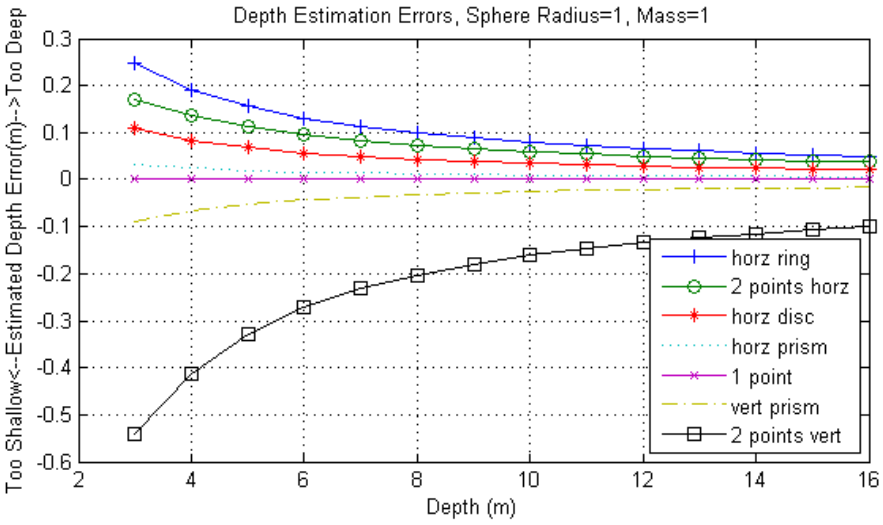

Fig. 9 Depth estimation errors of various distributions of a unit mass in a unit ball

Heuristically, we argue for the validity of the Claim 1 by citing Theorems 2 and 3 from Green (1952).

> Theorem 2: The greatest distance from the center of mass to an equipotential surface occurs when the generating mass of the admissible potential is from two equal point masses located on the boundary of the unit ball where the two points are aligned with the furthest point on the surface.
> Theorem 3: The closest point on an equipotential surface to the center of mass occurs when the generating mass is contained in an equatorial great circle with the closest point on the surface on a line through itself and the center of mass.

Empirically, we see in Fig. 9 how the ring and two vertical point mass distributions bound a variety of arbitrary mass distributions contained in the unit ball. Thus, even if a counter example is found and Claim 1 is proven false, it still has practical utility for our purposes.

One can also define *DC* in any Tangent Plane (TP) to the equipotential surface normal to the *Z* axis, as the product of U_z and the difference between maximum and minimum curvatures in TP (k_1 and k_2 respectively) (Slotnick 1932).

$$DC = U_z(k_1 - k_2). \qquad 14$$

We also note that the ring is the least concentrated mass arrangement on the equatorial great circle producing relatively small U_z values. The equations for the gradients of the ring are quite complicated

(Lass and Blitzer 1983), but we have found that a circular array of point masses provides a good approximation. Note, the maximum DC of the ring and two vertical points configurations occur respectively farthest from and closest to the origin of the computational plane as illustrated in Fig. 10. These facts motivated the development of Claim 1.

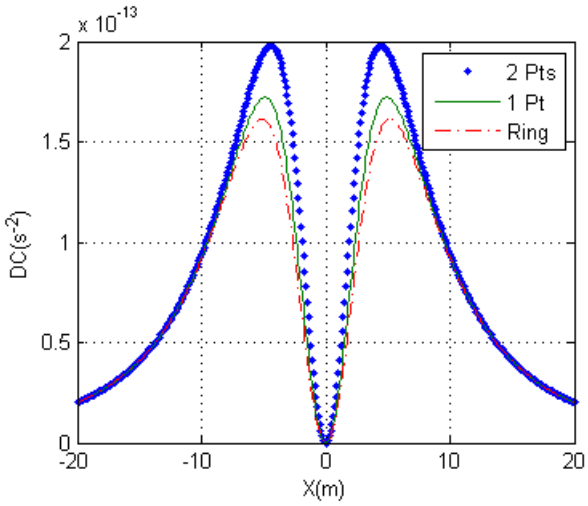

Fig. 10 DC for ring, 1 point, and 2 point masses rotated 10 deg from the vertical at 6m depth

Fig. 11 shows the orientation of two point masses on the boundary that produce the largest $||DC||_{sup}$ values as a function of depth. The orientation approaches vertical as depth approaches 1 and appears to be asymptotic to approximately 12 degrees as depth approaches infinity. In most practical applications, a vertical orientation provides an effective upper bound.

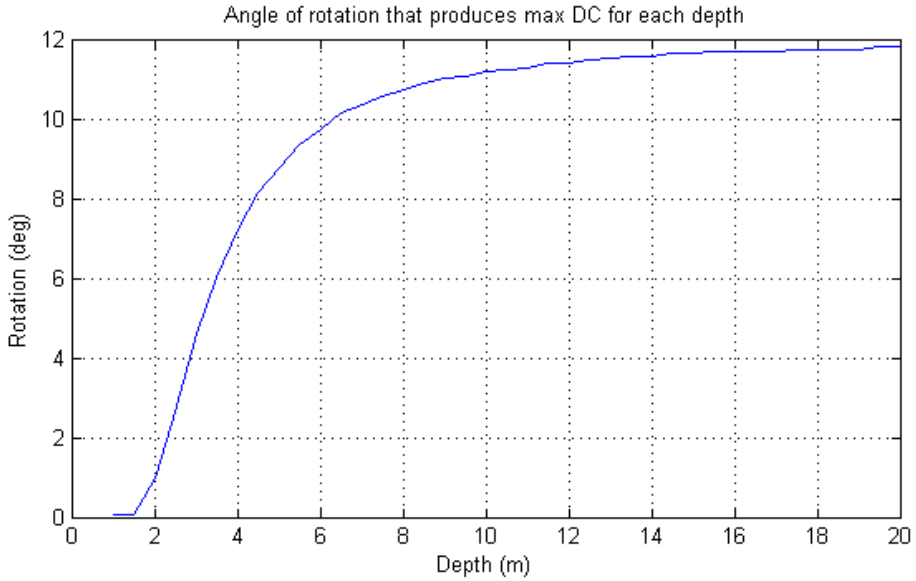

Fig. 11 Angle from vertical at which two points produce the max $||DC||_{sup}$ as a function of depth

We now consider an example in which we compute bounds for the unknown's mass and depth (center of mass) using Eq. 12 and Claim 1. For this example, we use a prism 3x10x3m at a depth of 15m. Given an observed maximum *DC* of $2.16 \times 10^{-9} s^{-2}$, we assume the object that generated this *DC* can be enclosed in a ball with radius 5.5m. We position point masses at the top and bottom of the ball and use Eq. 12 to determine the mass and depth combinations that produce the same maximum *DC*. We repeat this process using a ring at the ball's equator. The result is a pair of curves that bound the depth and mass of the unknown, represented by the dashed lines in Fig. 12.

Reading from Fig. 12, we can see the depth range attributed to the inverse solution with a mass determined from Fig. 8. For an object with an MMB solution mass of 2.07×10^{5}kg, the depth to the center of mass, *D*, falls in the range -13.7m>*D*>-18.1m based on the mass distributions as discussed in Claim 1.

If we assume a maximum error signal of $\pm 7 \times 10^{-10} s^{-2}$ and apply this to the DC value used to compute the depth, we get the bounds represented by the solid curves in Figure 12.

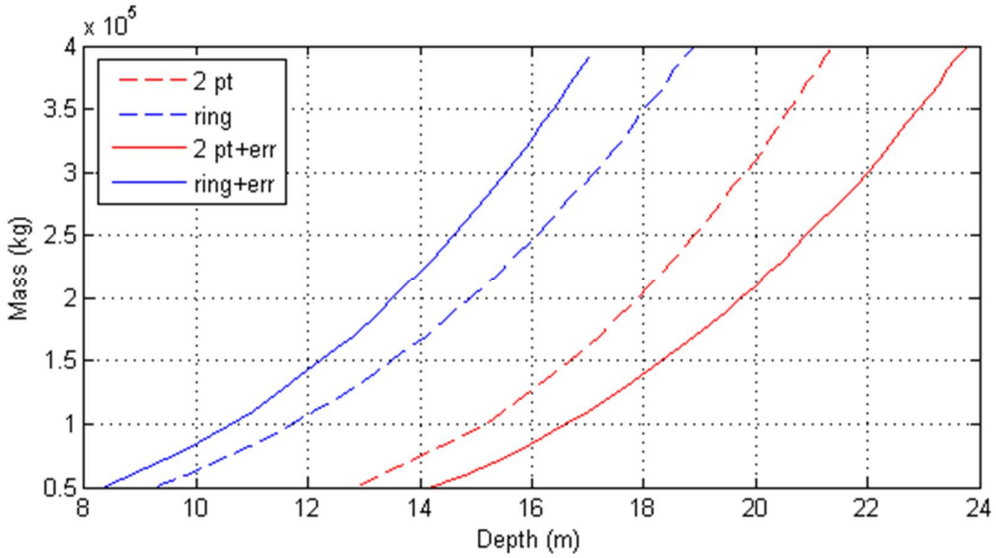

Fig. 12 Relationship between depth and mass for two vertical points (lower right) and a ring (upper left) on a ball with radius 5.5m. Dashed lines represent bounds with no measurement error. Solid lines represent bounds with $7 \times 10^{-10} s^{-2}$ measurement error.

The depth bounds calculated above will be wider for shallower, less spherical mass distributions than those we calculated from Eq. 12. The bounds will approach each other as depth increases with a fixed bounding ball as all distributions will then resemble a point mass from the observational plane.

4 Conclusion

In conclusion, we presented an algorithm (the MMB) that may be less susceptible to false positives in geophysical prospecting applications than those approaches relying solely on methods selecting inverse solution models that most closely fit the observed gradient data. This is true since the MMB algorithm produces solutions that have the same horizontal center of mass as the unknown and that ensure the anomaly (difference between inverse solution mass and unknown mass) has approximately the same amounts of positive and negative mass. Additionally, we presented tools for bounding possible locations of the unknown center of mass and total mass for strictly positive (or negative) mass. These bounds alert us to the condition when the size of the unknown mass may be small in relation to the noise in the particular inverse problem, increasing the danger of an ill-posed problem and increasing the likelihood of false positives or negatives.

While this analysis assumed a dense, regularly spaced array of observations, future work will examine the application of the approaches presented here to sparse observations sets.

Conflict of Interest: The authors declare that they have no conflict of interest.

References:

Anderson, R.: Analysis of gradiometer tensor fields of anomalous mass distributions. Saint Louis University (2011)

Difrancesco, D.: Advances and challenges in the development and deployment of gravity gradiometer systems, EGM 2007 International Workshop (2007)

Dransfield, M.: Airborne gravity gradiometry. University of Western Australia. (1994)

Freeden, W. and Nutz, H.: Satellite gravity gradiometry as tensorial inverse problem, Int J Geomath (2011). doi: 10.1007/s13137-011-0026-x

Green, J.W.: On the level surfaces of potentials of masses with fixed center of gravity, Pacific Journal of Mathematics, Vol 2, 147-152 (1952)

Jekeli, C.: A wavelet approach to the terrain correction in gravimetry and gravity gradiometry, Int J Geomath (2012). doi: 10.1007/s13137-011-0028-8

Lass, H. and Blitzer, L.: The gravitational potential due to uniform disks and rings, Celestial Mechanics 30, 225-228 (1983)

McGuirk, J. et al.: Sensitive absolute gravity gradiometry using atom interferometry, Physical Review A, Vol 65, issue 3 (2002)

Murböck, M. et al.: GOCE gravity gradients: a new satellite observable, Proc of '4th International GOCE User Workshop', Munich, Germany, 31 March-1 April 2011 (ESA SP-696, July 2011)

Novák, P. and Tenzer, R.: Gravitational gradients a satellite altitudes in global geophysical studies, Surv Geophys (2013). doi: 10.1007/s10712-013-9243-1

Romaides, A., et al.: A comparison of gravimetric techniques for measuring subsurface void signals. Journal of Physics D: Applied Physics (34-3) 433-443 (2001)

Slotnick, M.M.: Curvature of equipotential surfaces. American Association of Petroleum Geologists Bulletin, Vol. 16, 1250-1259 (1932)

Strogatz, S.: Nonlinear Dynamics and Chaos. Westview Press, Cambridge. (1994)

Uzun, S., and Jekeli, C.: comparison of least squares and simulated annealing to estimate fault parameters from airborne gravity gradiometry, Stud Geophys. Geod., (2015). doi: 10.1007/s11200-014-0712-x